Research Article

Bakytgul Massalimova*, Vladislav Sadykov, Nurzada Totenova, Julia Fedorova, Tatyana Glazneva, Tamara Krieger, Vladimir Rogov, Arkady Ishchenko

Efficient and stable to coking catalysts of ethanol steam reforming comprised of Ni + Ru loaded on $MgAl_2O_4$ + $LnFe_{0.7}Ni_{0.3}O_3$ (Ln = La, Pr) nanocomposites prepared via cost-effective procedure with Pluronic P123 copolymer

https://doi.org/10.1515/chem-2024-0118
received September 9, 2024; accepted November 18, 2024

Abstract: Mesoporous $MgAl_2O_4$ + $LnFe_{0.7}Ni_{0.3}O_3$ (Ln = La, Pr) nanocomposites were prepared by a cost-effective one-pot procedure with the Pluronic P123 copolymer and Ni + Ru active components were supported on them by wet impregnation. The real structure of samples was studied by X-ray diffraction and transmission electron microscopy with energy-dispersive X-ray spectroscopy, surface properties were determined by Fourier transform infrared spectroscopy of adsorbed CO, reactivity was evaluated by temperature programmed reduction by H_2, and catalytic activity was tested in ethanol steam reforming (ESR). Disordering of the real structure of nanocomposite supports due to incorporation of transition metal cations into $MgAl_2O_4$ results in the development of a metal–support interface and domination of single surface metal centers. This provides a high catalytic activity in the ESR reaction in the intermediate temperature range ~550°C, close to that of the best known catalysts, and stability to coking. A higher activity for the Pr-containing catalyst is provided by the high reactivity of surface oxygen species bound with Pr cations.

Keywords: ethanol steam reforming, nanocomposite spinel + perovskite supports + Ni + Ru, one-pot synthesis with the Pluronic P123 copolymer, surface sites, FTIRS of adsorbed CO

1 Introduction

The transformation of bio-renewable fuels into syngas and hydrogen is now considered one of the most important problems of green energy production [1]. Ethanol is among the easily produced, cheap, and broadly available fuels; hence, its steam reforming is among the most popular methods of catalysis in this area [2]. In this reaction, traditional cost-effective steam reforming catalysts comprising Ni and/or Co supported on alumina, silica, or zeolites suffer from coking, leading to rapid deactivation of the catalyst [2]. Although Pt group metals possess higher activity and coking stability [2], their high price makes it impossible for practical application. This problem is solved by the design of nanocomposite catalysts composed of mixed oxide supports (with perovskite, fluorite, spinel structures, etc.) possessing high oxygen mobility and reactivity and ability to strongly interact with loaded nanoparticles of Ni or Ni-based alloys [3]. Coking stability is provided by the so-called bifunctional mechanism of reforming, where fuel molecules are activated on metal sites and oxidants on reduced support sites produce reactive oxygen surface species, which rapidly migrate to the metal–support interface and interact with activated fuel fragments producing syngas

* **Corresponding author: Bakytgul Massalimova,** Department of Chemistry and Chemical Technology, Manash Kozybayev North Kazakhstan University, Pushkin Str 86, 150000, Petropavl, Kazakhstan, e-mail: bkmasalimova@ku.edu.kz
Vladislav Sadykov: Federal Research Center, Boreskov Institute of Catalysis SB RAS, 630090 Novosibirsk, Russia; Department of Natural Sciences, Novosibirsk State University, 630090, Novosibirsk, Russia, e-mail: sadykov@catalysis.ru
Nurzada Totenova: Department of Chemistry and Chemical Technology, M. Kh. Dulaty Taraz Regional University, Taraz, 080000, Kazakhstan, e-mail: ms.nurzada.93kz@mail.ru
Julia Fedorova, Tatyana Glazneva, Tamara Krieger, Arkady Ishchenko: Federal Research Center, Boreskov Institute of Catalysis SB RAS, 630090 Novosibirsk, Russia
Vladimir Rogov: Federal Research Center, Boreskov Institute of Catalysis SB RAS, 630090 Novosibirsk, Russia; Department of Natural Sciences, Novosibirsk State University, 630090, Novosibirsk, Russia

and preventing their transformation into coke [4]. For realization of this mechanism, a developed metal–support interface is required. Among attractive synthesis procedures to provide such interface, ex-solution of metal nanoparticles (Ni, Co, etc.) from the complex oxides with perovskite, spinel, fluorite, etc. structures under reducing conditions is to be mentioned [5–7]. In this case, both the epitaxy of metal clusters with the surface of the support and their decoration by oxidic fragments provide a developed interface, which also helps to prevent sintering of Ni under reaction conditions. While for fluorite-like complex oxides such as $PrSmCeZrO_2$ doped with Ni, the specific surface area (SSA) remains sufficiently high, for perovskite-like oxides containing Mn, Fe, Cr, etc. cations in B positions, along with Ni and Ru, the SSA after calcination in the range of 700–900°C is ~4 to 7 m^2/g [8], which is not good for practical applications. The preparation of nanocomposites composed of perovskite (P) and fluorite (F) allows the stabilization of the surface area of catalysts after Ni segregation, apparently by hampering the migration of cations between perovskite nanodomains via the presence of fluorite nanodomains as barriers [9]. While the one-pot Pechini route of P + F nanocomposite synthesis has not allowed us to obtain nanodomains of the perovskite phase due to incorporation of transition metal cations into fluorite domains, it is possible to prepare nanocomposites containing perovskite nanodomains when fluorite nanopowders are dispersed in the perovskite polymeric precursor solution with subsequent evaporation and calcination [9].

Another approach to stabilize the dispersion of perovskite-based active components with Ni is to load it by simple wet impregnation on a mesoporous $MgAl_2O_4$ support prepared by a one-pot evaporation-induced self-assembly method. In this method, although incorporation of transition metal cations into the spinel lattice takes place, diffraction peaks of the perovskite phase were not observed even for supported 20 wt% $PrNi_{0.9}Ru_{0.1}O_3$ due to their small size and disordering of perovskite domains [10]. Along with reactive surface oxygen species provided by supported perovskite layers, the presence of Mg in this spinel support also helps to suppress coking due to the decreasing density of acid sites responsible for ethylene formation and coke generation [2,4,10,11].

To further simplify the preparation procedure, one-pot synthesis seems interesting, where in the preparation of mesoporous materials with the help of the Pluronic P123 copolymer [10] all cations of perovskite can be mixed with Mg and Al cations in one solution, and then a typical procedure for mesoporous material synthesis will be applied. There is no doubt that part of the transition metal cations will be incorporated into the $MgAl_2O_4$ lattice. Hence, to guarantee the presence of perovskite phases in nanocomposites with $MgAl_2O_4$, their content has to be rather high, up to ~50 wt%. The critical point of this nanocomposite synthesis procedure is that due to the presence of high concentrations of Ln and transition metal cations in solution, formation of the $MgAl_2O_4$ spinel phase could not be ensured, and to date it is not checked anywhere. Since doping of $MgAl_2O_4$ by Fe, Cr, and Ti cations was already demonstrated to be a good option for the increase of supported nanocomposite activity and stability in fuel reforming into syngas [11], testing this promising procedure in the synthesis of nanocomposites composed of perovskites $LaFe_{0.7}Ni_{0.3}O_3$ or $PrFe_{0.7}Ni_{0.3}O_3$ with $MgAl_2O_4$ is worth trying, which is the purpose of this article. Its successful application opens up a new route for manufacturing efficient, stable to coking, and cost-effective catalysts for biofuel transformation into syngas and hydrogen for the efficient development of the green energy field. The absence of any liquid waste in this synthesis procedure makes its industrial application very attractive.

2 Materials and methods

2.1 Catalyst preparation

The following reagents were used in the synthesis: P123 Pluronic triblock copolymer $((EO)_{20}(PO)_{70}(EO)_{20}$ (M_n = 5,800, Sigma Aldrich), aluminum isopropoxide ($Al(OPri)_3$, Acros Organics), HNO_3 (REACHIM), $Ni(NO_3)_2{\cdot}6H_2O$ (Acros Organics), $Mg(NO_3)_2{\cdot}6H_2O$ (REACHIM), and $Pr(NO_3)_3{\cdot}nH_2O$ (Vecton). The synthesis procedure is described in detail with an example of the first nanocomposite. The first solution was prepared by adding 60 mL of EtOH to 6.0 g of Pluronic P123 and stirring with a magnetic stirrer for 1 h. The second solution was prepared by adding 30 mL of EtOH and 2 mL of HNO_3 to 8.61 g of aluminum isopropoxide and stirring for 1 h. Then, the two solutions were mixed and after stirring for 0.5 h 5.37 g of $Mg(NO_3)_2{\cdot}6H_2O$ were added. After stirring for 0.5 h, 2.96 g of Fe nitrate and 0.72 g of $Pr(NO_3)_3{\cdot}nH_2O$ were added and stirred for 3 h, then the resulting solution was dried at 60°C for 72 h. A dried polymeric mixture was placed into a tubular reactor and heated in a stream of air with the heating rate of 1° per minute to 700°C and kept at this temperature for 5 h. 5% Ni + 1% Ru were supported by the impregnation method using mixed solutions of $Ni(NO_3)_2{\cdot}nH_2O$ (Vecton) and crystalline anhydrous $RuOCl_3$ (Reakhim), followed by drying and calcination at 700°C for 1 h. All reagents were of analytical pure grade and used without any pretreatment.

2.2 Catalyst characterization

Diffraction patterns were obtained using a Bruker Advance D8 diffractometer with CuKα radiation (γ, 1.5418 Å). Scanning

was performed in the range of 15–90° (2θ) with a scanning step of 0.05 (2θ) and an accumulation time of 3 s.The diffractograms were processed using the EVA program included in the diffractometer software package for identification of the obtained phases.

High-resolution transmission electron microscopy images were obtained with a JEM-2200FS transmission electron microscope (JEOL Ltd., Japan; acceleration voltage, 200 kV; lattice resolution, 1 Å) equipped with a Cs-corrector and an EDX spectrometer (JEOL Ltd., Japan). The samples for the TEM study were prepared by ultrasonic dispersion in ethanol and consequent deposition of the suspension on a "holey" carbon film supported on a copper grid. The minimum spot diameter for the step-by-step line or mapping elemental energy-dispersive X-ray spectroscopy (EDX) analysis was ~1 nm with a step of about 1.5 nm.

The SSA of samples was evaluated by the Brunauer–Emmet–Teller (BET) method by recording physical adsorption of nitrogen at the liquid nitrogen temperature using an ASAP-2400 (Micromeritics Instrument. Corp., Norcross, GA, USA) automated volumetric adsorption unit. Before the analysis, samples were outgassed at 150°C for 4 h at a pressure of 1×10^{-3} Torr (~0.1 Pa). The obtained adsorption isotherms were used to calculate the SSA and pore size distribution.

The surface properties of samples were studied using low-temperature Fourier transform infrared spectroscopy (FTIRS) of adsorbed carbon monoxide (CO), which was earlier efficiently used in our works to estimate the density and local structure of surface metal sites [4,10,11]. Samples were pressed into pellets with a size of $1 \times 2\ cm^2$ and a weight of 40 mg, then put into the IR cell and heated in a vacuum to 500°C, followed by H_2 addition to 200 Torr and reducing for 1 h at this temperature. Then, the cell was evacuated up to a residual pressure of below 10^{-4} Torr and cooled to room temperature. Spectra were registered on a Shimadzu IRTracer-100 spectrometer in the range of 400–6,000 cm^{-1} with a resolution of 4 cm^{-1} and accumulation of 200 scans. CO was adsorbed at −196°C and CO pressure from 0.1 to 10 Torr. After recording spectra at −196°C, the cell was heated to room temperature and spectra were registered. These spectra recorded in the absorption scale were normalized to the optical thickness of a pellet, and the spectrum before CO adsorption was subtracted from that after CO adsorption. Spectral analysis was carried out

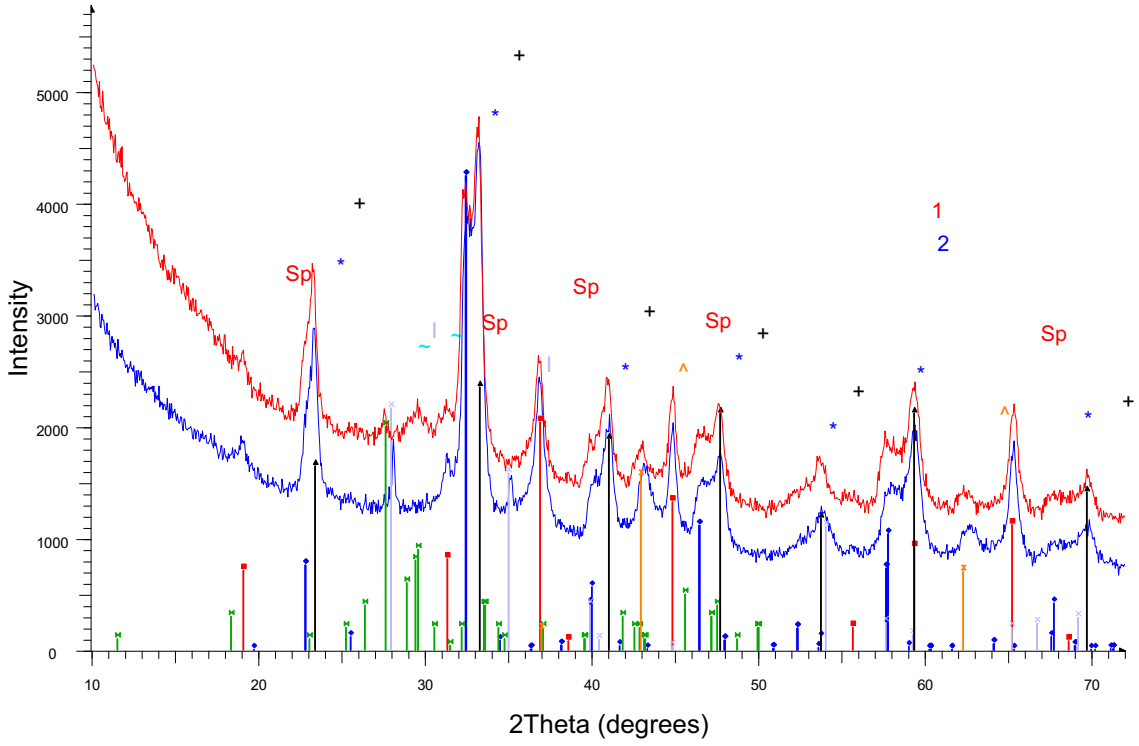

Figure 1: XRD patterns of the nanocomposite support 50% $MgAl_2O_4$ + 50% $LaFe_{0.75}Ni_{0.25}O_3$ (1) and the 5% Ni + 1% Ru/(50% $MgAl_2O_4$ + 50% $LaFe_{0.75}Ni_{0.25}O_3$) catalyst (2). Sp – $MgAl_2O_4$ [PDF 00-021-1152], * – $LaFe_{0.75}Ni_{0.25}O_3$ [PDF 01-088-0630], + – $LaNiO_3$ [PDF 00-033-0710], ^ – MgO-NiO [PDF 01-078-0430 MgO], | – RuO_2 [PDF 03-065-2824], and ~ – $La_{10}Al_4O_{21}$ [PDF 00-039-0009]. Moreover, positions of some phases in diffraction peaks are marked by lines.

by deconvolution of the corresponding IR bands on individual Gaussian components. Concentrations of different adsorption centers were estimated from the integral intensities of observed characteristic absorption bands using integral absorption coefficients [12].

Material reactivity was characterized by temperature-programmed reduction by H_2 (TPR-H_2) (10% H_2 in Ar; feed rate: 2.5 L/h; temperature ramp: from 25 to 900°C at 10 °C/min) in a flow kinetic setup with a quartz U-shaped reactor equipped with a Tsvet-500 chromatograph and a thermal conductivity detector.

2.3 Catalyst testing in ethanol steam reforming (ESR)

ESR was conducted in a continuous-flow fixed-bed quartz reactor under atmospheric pressure in the temperature range of 550–700°C. A total of 30 mg of catalyst (0.25–0.5 mm fraction) was loaded and sandwiched between two quartz wool layers. Prior to the activity test, the catalyst was reduced with 5 vol% H_2/Ar (100 mL/min) at 650°C for 1 h. The EtOH and H_2O mixture was heated to 120°C and mixed with N_2 stream coming from the mass-flow controller, yielding a typical feed gas composition of EtOH/H_2O = ¼, where C(EtOH) = 2% vol. The outlet products were analyzed by gas chromatography using a Tsvet-500 chromatograph. To ensure fast steady-state achievement, experiments were started at 700°C, kept for 1 h at this temperature, and then decreasing it to 550°C in steps of 50°C keeping for 1 h at each step.

3 Results

3.1 Structural and textural properties

Figures 1 and 2 present diffraction patterns of studied samples. In both La-containing samples, the $MgAl_2O_4$ spinel phase [PDF 00-021-1152] with a crystallite size below 20 nm and lattice parameter 8.08 Å was identified. Two perovskite phases corresponding to $LaFe_{0.75}Ni_{0.25}O_3$ [PDF 01-088-0639] and $LaNiO_3$ [PDF 00-033-0710] were observed. In both patterns, broad diffraction peaks were also present corresponding to the cubic Fm-3m structure of Mg(Ni)O with lattice parameters 4.213 and 4.182 Å for the support and the catalyst, respectively. Moreover, in the support, the

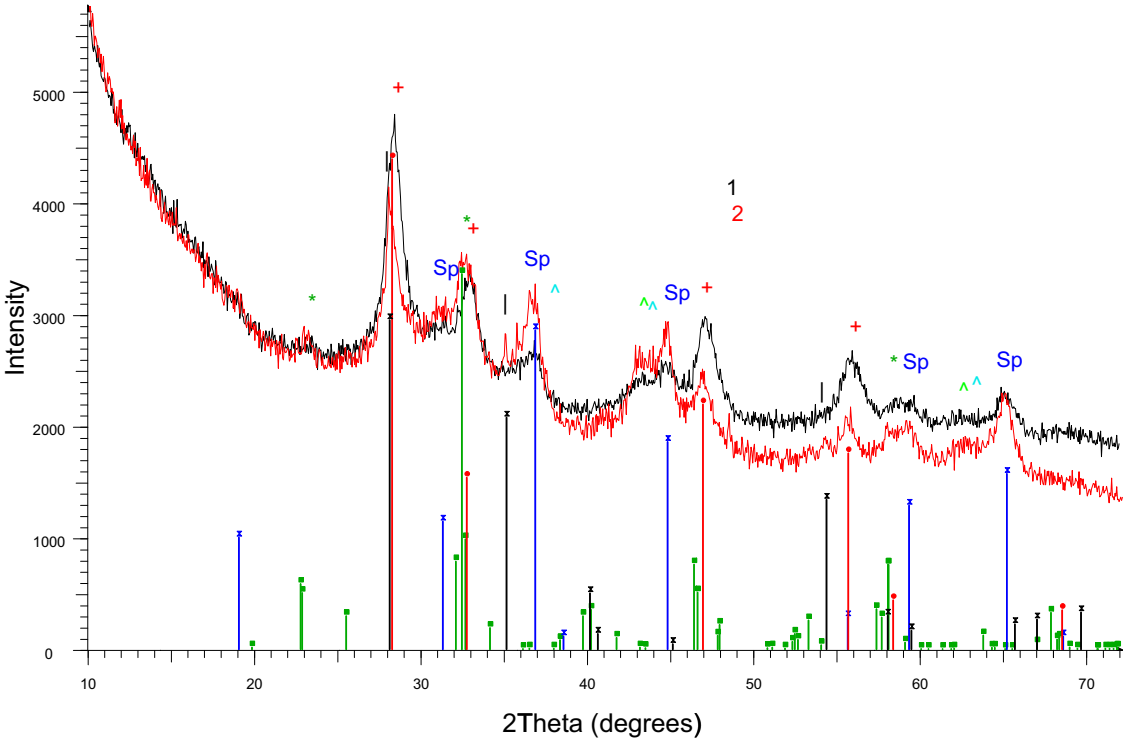

Figure 2: XRD patterns of the nanocomposite support 50% $MgAl_2O_4$ + 50% $PrFe_{0.75}Ni_{0.25}O_3$ (1) and the 5% Ni + 1% Ru/(50% $MgAl_2O_4$ + 50% $PrFe_{0.75}Ni_{0.25}O_3$) catalyst (2). Sp – $MgAl_2O_4$ [PDF 00-021-1152], * – perovskite [PDF 01-074-1472], + – PrO_2 [PDF 00-006-0329], ^^ – MgO-NiO [PDF 01-078-0430 MgO], and | – RuO_2 [PDF 03-065-2824]. Moreover, positions of some phases in diffraction peaks are marked by lines.

$La_{10}Al_4O_{21}$ phase [PDF 00-039-0009] was observed, which is absent after supporting Ni and Ru oxides due to interaction with the impregnating solution. Pr-containing samples (Figure 2) were characterized by broader diffraction peaks compared with La-containing samples (Figure 1), indicating a higher disorder. It is reflected in smaller (9–12 nm) size $MgAl_2O_4$ spinel phase domains, while diffraction peaks corresponding to the perovskite phase are very weak or absent. This correlates with the presence of strong PrO_2 diffraction peaks with domain sizes of ~9 to 11 nm, thus indicating instability of the perovskite $PrFe_{0.75}Ni_{0.25}O_3$ phase in combination with the $MgAl_2O_4$ spinel phase due to incorporation of transition metal cations into the spinel lattice [11]. After loading NiO + RuO_2, the intensity of PrO_2 peaks decreases, apparently due to the formation of disordered praseodymium nickelate fragments, while the appearance of RuO_2 peaks indicates that Ru is in part deposited as RuO_2 nanoparticles. Similar to the case of samples with La, in Pr-containing samples, the Mg(Ni)O solid solution phase (domain sizes below 15 nm) is present as well.

TEM images of catalyst samples are presented in Figures 3 and 4.

For both types of catalysts, the particles are composed of stacked nanodomains of different orientations and disordering degrees, apparently corresponding to different phases in agreement with XRD data.

Figure 5 presents the particle size distribution for these catalysts from TEM data. The smaller sizes of particles of the Pr-containing sample agree with XRD data (vide supra).

EDX data (Figure 6, Table 1) for the 5% Ni + 1% Ru/(50% $MgAl_2O_4$ + 50% $LaFe_{0.75}Ni_{0.25}O_3$) catalyst demonstrate rather moderate spatial variation of the Ni concentration in the surface layer of the nanocomposite, which is good for ensuring reproducibility of catalytic properties. Note that for the $LaMn_{0.45}Ni_{0.45}Ru_{0.1}O_3$ + $Pr_{0.15}Sm_{0.15}Ce_{0.35}Zr_{0.35}O_2$ nanocomposite prepared by a one-pot Pechini route [9], strong spatial variation of the Ni content and hence the degree of Ni agglomeration and interaction with the support resulted in low catalytic activity. A high content of Ru revealed in Figure 4d (Table 1) is apparently due to the presence of RuO_2 particles in agreement with XRD data (Figure 1). A high content of Mg in all places also agrees with the presence of the NiO-MgO phase, as revealed by XRD, which provides a strong

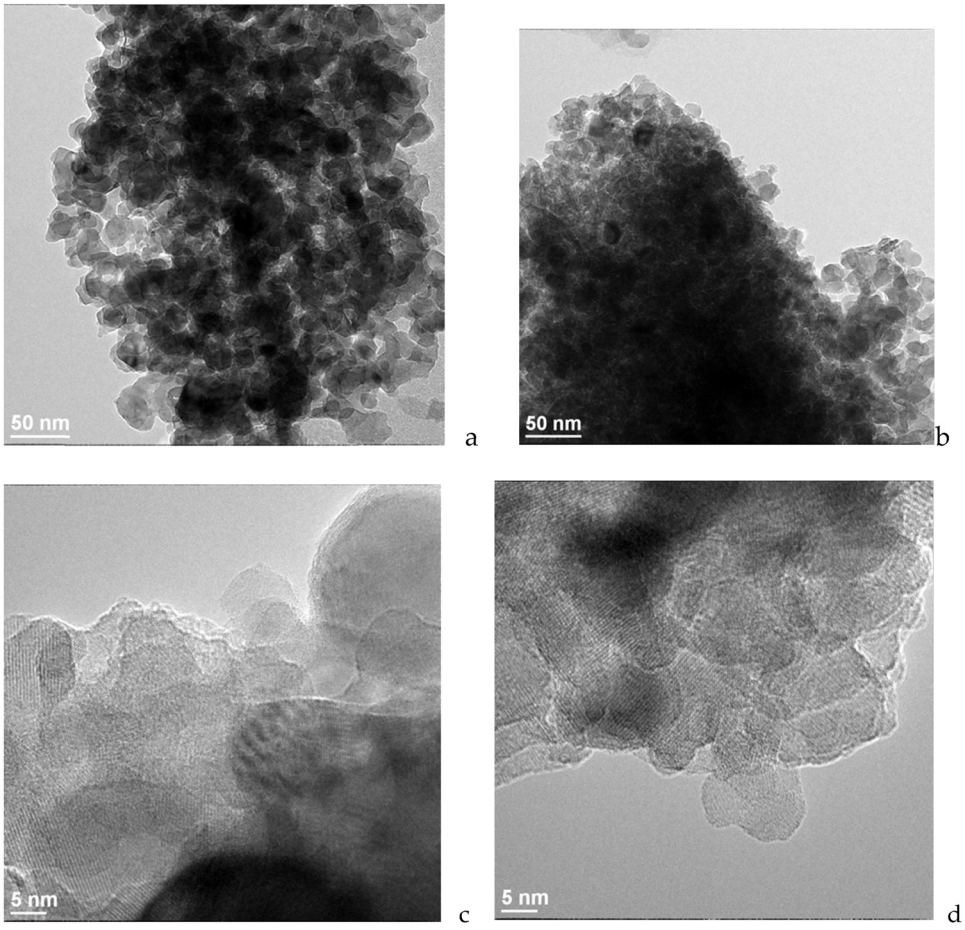

Figure 3: TEM images of the typical regions (a–d) of 5% Ni + 1% Ru/(50% $MgAl_2O_4$ + 50% $PrFe_{0.75}Ni_{0.25}O_3$) catalyst.

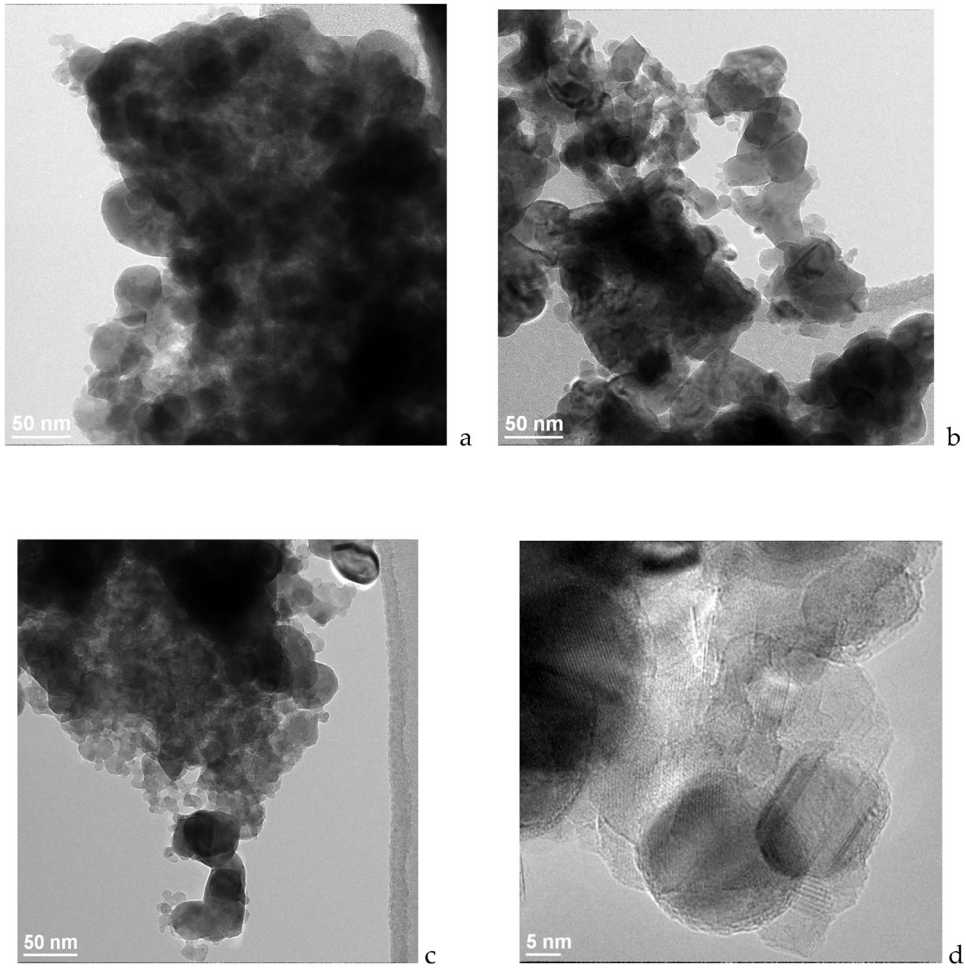

Figure 4: TEM images of the typical regions (a–d) of 5% Ni + 1% Ru/(50% $MgAl_2O_4$ + 50% $LaFe_{0.75}Ni_{0.25}O_3$) catalyst.

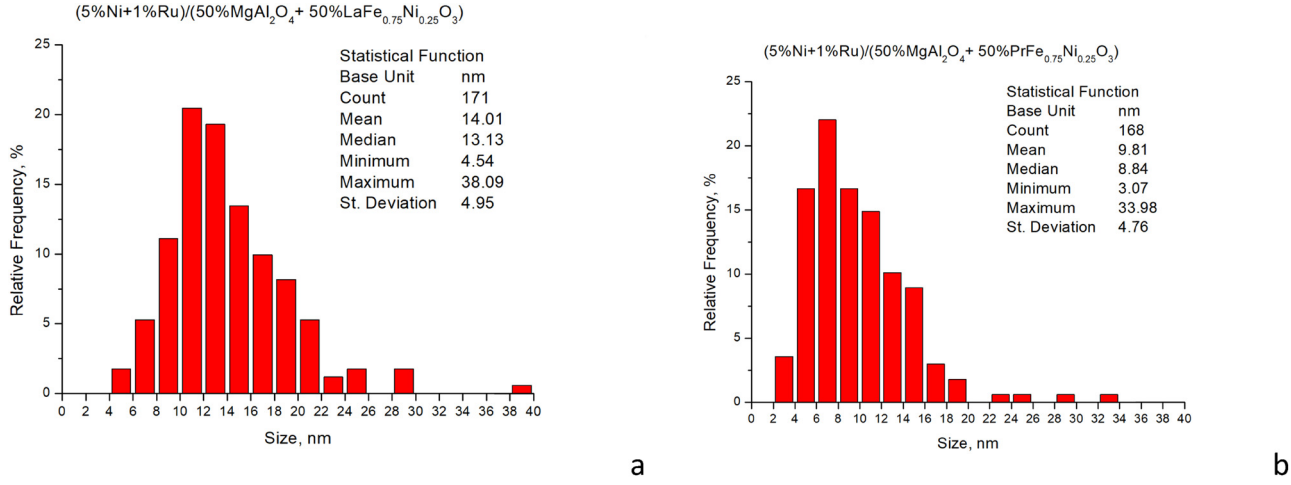

Figure 5: Particle size distribution for (5% Ni + 1% Ru)/(50% $MgAl_2O_4$ + 50% $LaFe_{0.75}Ni_{0.25}O_3$) (a) and (5% Ni + 1% Ru)/(50% $MgAl_2O_4$ + 50% $PrFe_{0.75}Ni_{0.25}O_3$) (b) catalysts. (Calculated from a pool of different TEM photos at the same magnification using the ImageJ program.).

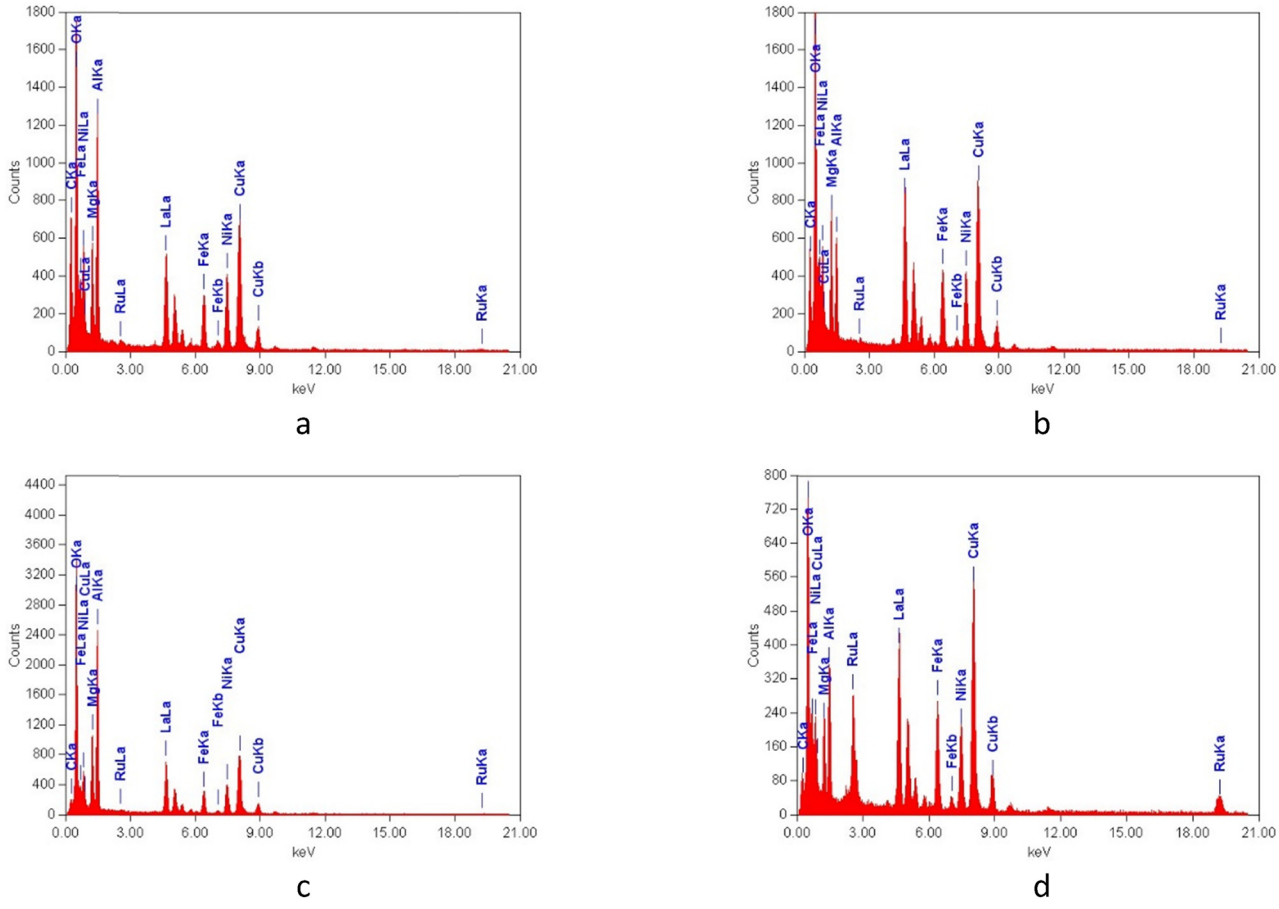

Figure 6: EDX spectra of 5% Ni + 1% Ru/(50% $MgAl_2O_4$ + 50% $LaFe_{0.75}Ni_{0.25}O_3$) catalyst particles in regions a–d in Figure 4.

Table 1: EDX data on the elemental composition of 5% Ni + 1% Ru/(50% $MgAl_2O_4$ + 50% $LaFe_{0.75}Ni_{0.25}O_3$) catalyst particles in regions a–d in Figure 6

Region in Figure 4	Concentration of elements by EDX, at (%)					
	Ni	Ru	La	Fe	Mg	Al
a	16.1	0.7	17.1	11.0	16.9	38.2
b	16.9	0.8	27.4	15.4	22.9	16.6
c	10.5	0.4	13.7	6.9	20.5	47.9
d	15.9	15.5	23.3	15.6	11.9	17.8

Ni–support interaction required for suppressing coking. Since according to XRD data (vide supra) for the 50% $MgAl_2O_4$ + 50% $PrFe_{0.7}Ni_{0.3}O_3$ nanocomposite, the perovskite phase was absent due to strong incorporation of Ni and Fe cations into the spinel lattice, and the SSA is higher (vide infra), while the Mg(Ni)O solid solution phase is present in the catalyst, even more uniform distribution of Ni on the catalyst surface is expected, which agrees with EDX mapping (Figure 7).

Figure 8 illustrates nitrogen adsorption isotherms and pore size distribution for catalysts, and Table 2 presents data on their SSA, pore size distribution, and average pore diameter. Adsorption curve hysteresis demonstrates the presence of mesopores, especially for the La-containing catalyst. For the Pr-containing catalyst, apparently, a combination of micropores with macropores is present. TEM images of pores in these catalysts (Figure 9) show that pore sizes reasonably agree with values obtained by analysis of adsorption isotherms. SSA values are reasonably high, though being lower than those for catalysts based on doped $MgAl_2O_4$ with supported active components, where values ~100 m^2/g were obtained [11]. Hence, as expected, transition metal and rare earth cations apparently help with the sintering of $MgAl_2O_4$ spinel nanodomains. However, SSA values are better than those of catalysts based on perovskite–fluorite nanocomposites with SSAs ~20 m^2/g [9].

3.2 Surface properties

Identification of the surface sites and characterization of their properties were carried out by FTIRS using CO as the

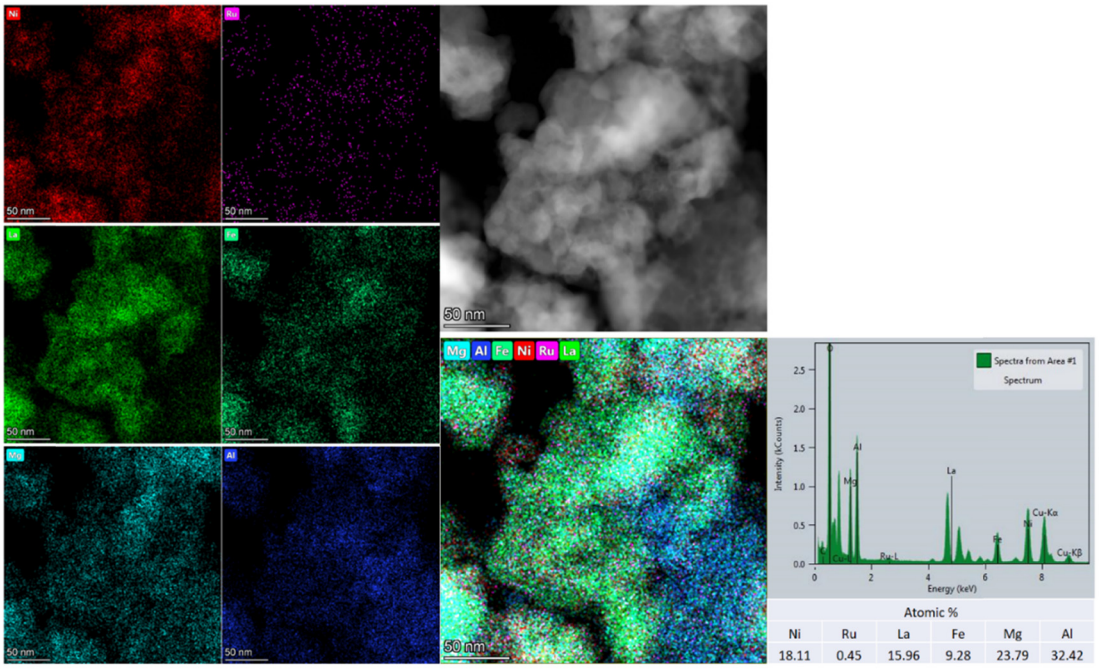

a

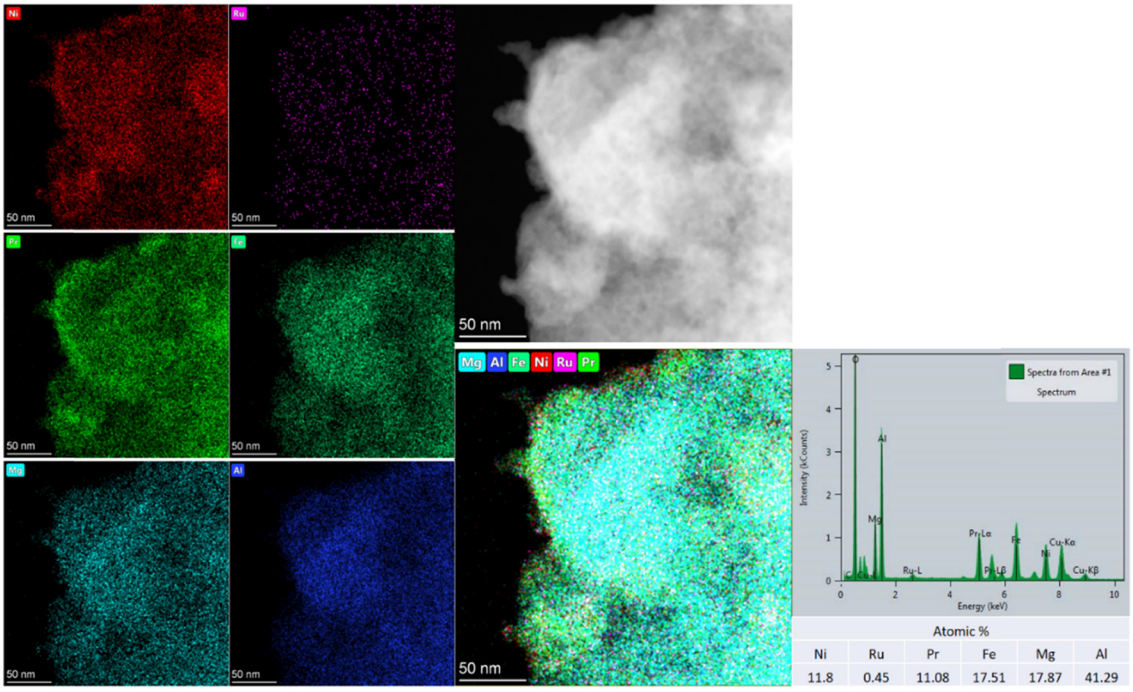

b

Figure 7: Typical HAADF-STEM images and EDX mapping for (5% Ni + 1% Ru)/(50% $MgAl_2O_4$ + 50% $LaFe_{0.75}Ni_{0.25}O_3$) (a) and (5% Ni + 1% Ru)/(50% $MgAl_2O_4$ + 50% $PrFe_{0.75}Ni_{0.25}O_3$) (b) catalysts.

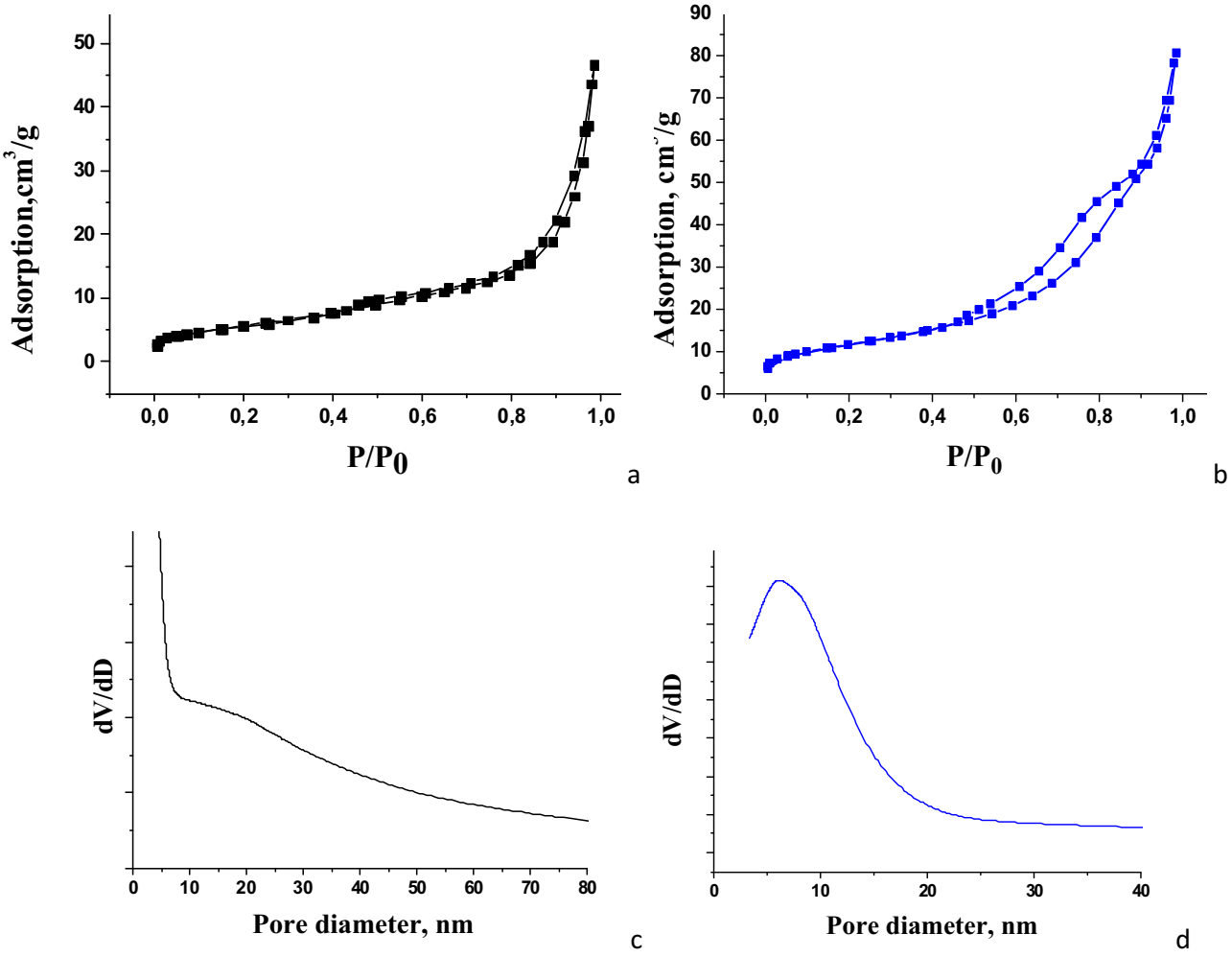

Figure 8: Adsorption isotherms and pore size distribution for (5% Ni + 1% Ru)/(50% $MgAl_2O_4$ + 50% $PrFe_{0.75}Ni_{0.25}O_3$) (a, c) and (5% Ni + 1% Ru)/(50% $MgAl_2O_4$ + 50% $LaFe_{0.75}Ni_{0.25}O_3$) (b, d) catalysts.

test molecule. Figure 10 presents spectra of CO adsorbed on 50% $MgAl_2O_4$ + 50% $LaFe_{0.7}Ni_{0.3}O_3$ at −196°C with pressure variation from 0.1 to 10 Torr. Bands at 2,148 and 2,160 cm^{-1} correspond to CO adsorption on different cations and OH-groups, while the band at 2,139 cm^{-1} can be assigned to physically adsorbed CO [13,14]. Low intensity bands at 2,065 and 2,080 cm^{-1} correspond to CO complexes with metal sites, apparently, Ni^0 [15,17].

The band at 2,080 cm^{-1} shifts to 2,090 cm^{-1} with the increase of CO pressure. After heating the sample to room temperature, the bands of adsorbed CO were not revealed.

Figure 11 presents spectra of CO adsorbed on the (5% Ni + 1% Ru)/$MgAl_2O_4$ + $LaFe_{0.7}Ni_{0.3}O_3$ sample at −196°C and 0.1–10 Torr CO pressure. Bands at 2,158 and 2,170 cm^{-1} characterize CO adsorption on the support centers, while bands at 1,945, 2,045, and 2,080 cm^{-1} correspond to CO adsorbed on metal sites [13–15].

Bands at 2,045 and 2,080 cm^{-1} are due to terminal CO complexes, while the band at 1,945 cm^{-1} refers to bridging

Table 2: Textural characteristics of samples

Sample	SSA (m^2/g)	V_{pores} (cm^3/g)	D_{av} (nm)
(5% Ni + 1% Ru)/50% $MgAL_2O_4$ + 50% $LaFe_{0.7}Ni_{0.3}O_3$	42	0.13	12
(5% Ni + 1% Ru)/50% $MgAl_2O_4$ + 50% $PrFe_{0.7}Ni_{0.3}O_3$	83	0.07	14

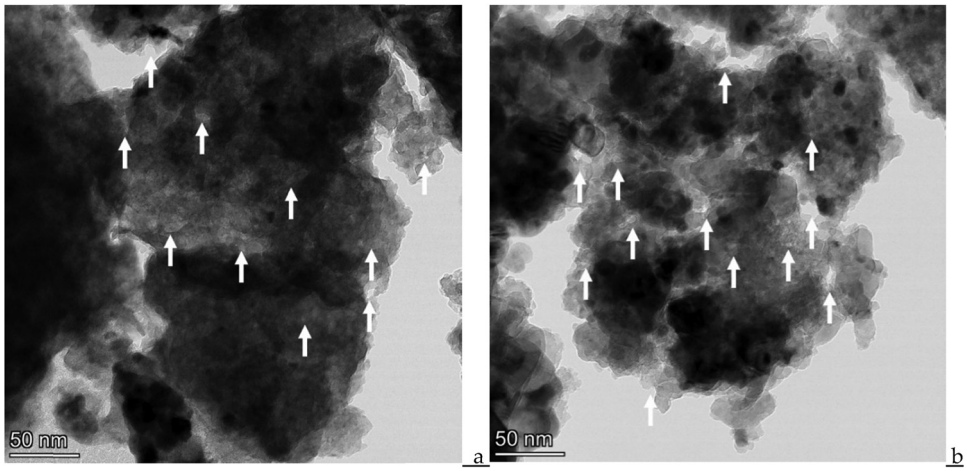

Figure 9: Typical TEM images of the porous structure (5% Ni + 1% Ru)/(50% $MgAl_2O_4$ + 50% $PrFe_{0.75}Ni_{0.25}O_3$) (a) and the (5% Ni + 1% Ru)/(50% $MgAl_2O_4$ + 50% $LaFe_{0.75}Ni_{0.25}O_3$) (b) catalyst [pores indicated by arrows].

carbonyls [16,17]. As expected, the intensity of bands corresponding to CO adsorbed on metal sites for the supported Ru + Ni catalyst is much higher than that for the initial 50% $MgAl_2O_4$ + 50% $LaFe_{0.7}Ni_{0.3}O_3$ nanocomposite. After heating the sample from liquid nitrogen temperature to room temperature, a broad band with a maximum at 2,065 cm^{-1} remains in the spectrum (Figure 12). Deconvolution of this band into Gaussian components revealed 4 bands with maxima at 1,965, 2,020, 2,050, and 2,073 cm^{-1}. The first band corresponds to the bridging form of CO adsorption on metal sites, while the other three refer to terminal complexes. The estimated concentration of metal sites is equal to 6 and 11 μmol/g for bridging and terminal carbonyls, respectively.

Figure 13 presents FTIR spectra of CO adsorbed on the Ni + Ru/$MgAl_2O_4$ + $PrFe_{0.75}Ni_{0.25}O_3$ sample at −196°C with pressure variation from 0.1 to 10 Torr. Bands at 2,158, 2,165, and 2,215 cm^{-1} characterize CO adsorption on support sites [13,14], while the bands at 2,040 and 2,080 cm^{-1} correspond to CO adsorbed on metal sites as terminal carbonyls [15–17]. The band at 2,080 cm^{-1} with the increase in CO pressure shifts to 2,090 cm^{-1}, which is typical for CO adsorbed in a linear configuration on metal planes.

When the sample was heated from the liquid nitrogen temperature to room temperature (Figure 14), the band with the maximum at 2,058 cm^{-1} remained in the FTIR spectrum.

Deconvolution of this band into Gaussian components revealed the bands with maxima at 1,995, 2,043, 2,058, and 2,080 cm^{-1}. The first band corresponds to bridging forms of

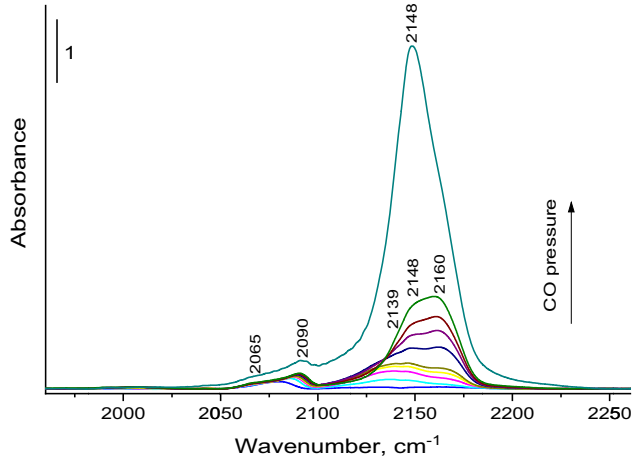

Figure 10: Spectra of CO adsorbed on the 50% $MgAl_2O_4$ + 50% $LaFe_{0.7}Ni_{0.3}O_3$ sample at −196°C and 0.1–10 Torr pressure.

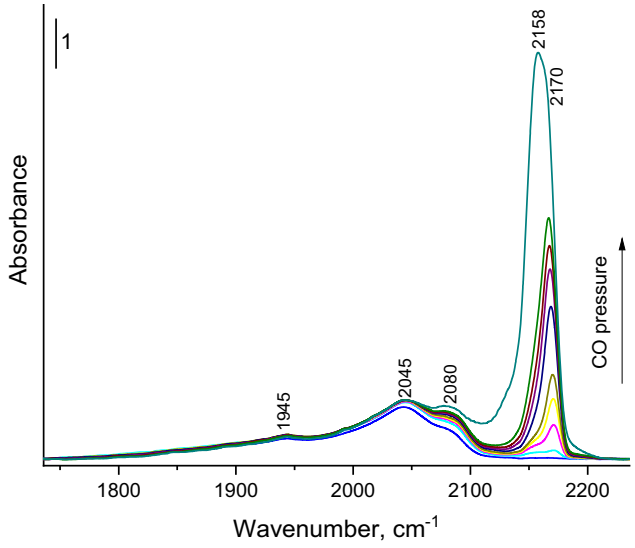

Figure 11: Spectra of CO adsorbed on the (5% Ni + 1% Ru)/50% $MgAl_2O_4$ + 50% $LaFe_{0.7}Ni_{0.3}O_3$ sample at −196°C and 0.1–10 Torr pressure.

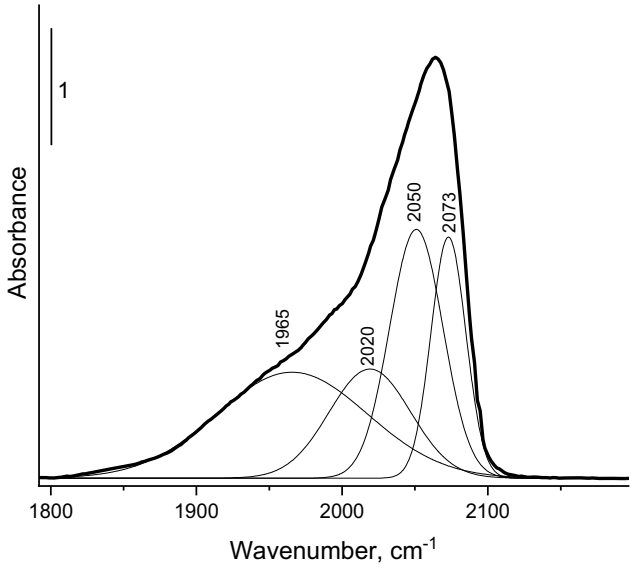

Figure 12: FTIR spectrum of CO adsorbed on the (5% Ni + 1% Ru)/50% $MgAl_2O_4$ + 50% $LaFe_{0.7}Ni_{0.3}O_3$ sample at room temperature and 10 Torr CO pressure; the decomposition into Gaussian components is shown.

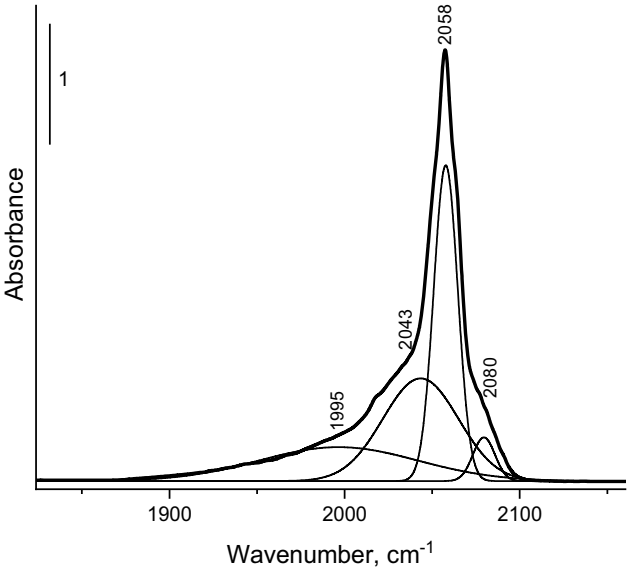

Figure 14: FTIR spectra of CO adsorbed on the Ni + Ru/50% $MgAl_2O_4$ + 50% $PrFe_{0.75}Ni_{0.25}O_3$ sample at room temperature and 10 Torr CO pressure.

CO adsorption on metal particles, while the other three to terminal ones on isolated metal sites with different local environments [15–18]. The estimated concentration of surface sites is equal to 3 and 11 μmol/g for bridging and terminal carbonyls, respectively. A higher share of terminal carbonyls for Pr-containing catalysts apparently correlates with a higher specific area as well as with a higher nanocomposite support disordering, which helps to provide a higher Ni and Ru dispersion and a higher degree of metal–support interaction, leading to decoration of the surface of Ni/Ru nanoparticles/clusters by oxidic fragments. Note that for both catalysts, the density of isolated metal sites stabilizing terminal carbonyls (11 μmol/g) is quite close to that for catalysts NiRu/PrCeZrO/$MgAl_{1.9}Me_{0.1}O_4$ (Me = Ti, Fe, Cr) (in the range of 9.5–14 μmol/g) with higher SSAs (85–110 m^2/g) at the same amount of supported metal 5% Ni + 1% Ru [11]. Hence, disordering of the surface layers of nanocomposite supports indeed helps to provide a high dispersion of supported metals and a high density of isolated metal sites even for the case of somewhat lower SSA.

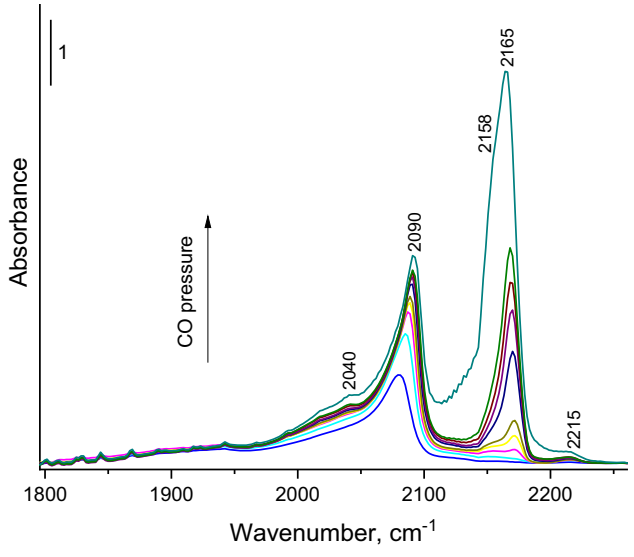

Figure 13: FTIR spectra of CO adsorbed on the Ni + Ru/50% $MgAl_2O_4$ + 50% $PrFe_{0.75}Ni_{0.25}O_3$ sample at −196°C and 0.1–10 Torr pressure.

3.3 H_2-TPR analysis

H_2-TPR curves for both catalysts (Figure 15) contain two narrow peaks in the range of 200–300°C corresponding to the reduction of RuO_2 and NiO nanoparticles and their mixed clusters conjugated with a reduction of Pr and Fe cations in the surface layer [9–11]. The higher intensity of the peak at ~250°C for the Pr-containing catalyst is explained by a smaller content of pure RuO_2 particles due to a stronger interaction between Pr and Ni oxidic species forming surface nanoparticles of Pr nickelates including Ru cations, as well as a high reactivity of surface oxygen species bound with Pr^{4+} cations. Broad peaks in the range of 400–900°C are related to the reduction of both perovskite phases, NiMgO phase, as well as Fe and Ni cations incorporated into the bulk of

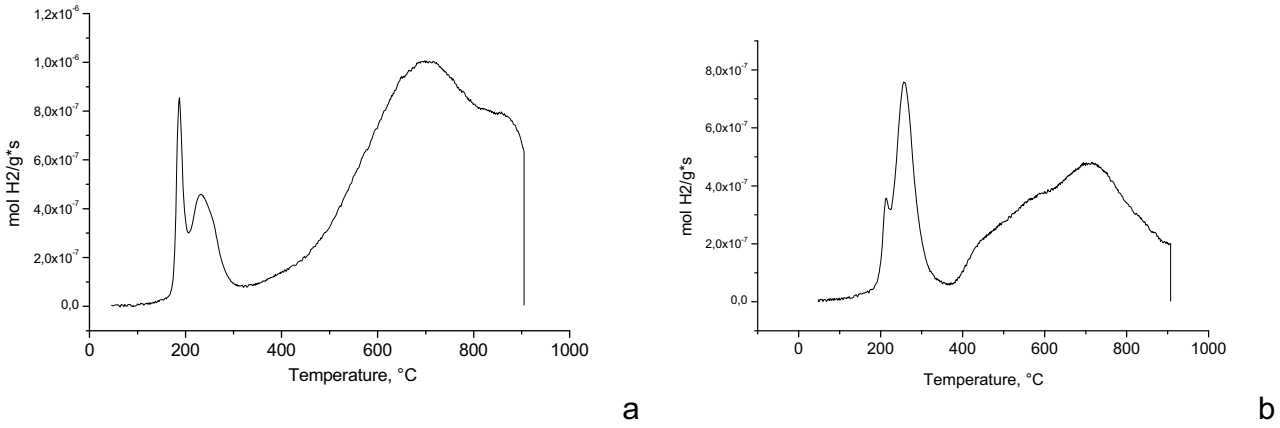

Figure 15: H_2 TPR curves for (5% Ni + 1% Ru)/50% $MgAl_2O_4$ + 50% $LaFe_{0.7}Ni_{0.3}O_3$ (a) and (5% Ni + 1% Ru)/50% $MgAl_2O_4$ + 50% $PrFe_{0.75}Ni_{0.25}O_3$ (b) catalysts.

$MgAl_2O_4$ particles [9–11]. The lower intensity of this peak for the Pr-containing catalyst apparently correlates with the absence of the bulk $PrFe_{0.75}Ni_{0.25}O_3$ phase in the support.

3.4 Catalytic activity

Figures 16 and 17 present temperature dependencies of ESR product concentrations. At each temperature, the performance was stable not suffering from any decline, which is explained by coking and sintering stability typical for nanocomposite active components based on mesoporous $MgAl_2O_4$. Hence, a one-pot synthesis route of nanocomposites used in this work has not deteriorated such important advantage of these catalysts. At 550°C, the concentration of hydrogen is higher for the Pr-containing catalyst, which correlates with a higher share of CO_2 in products. This can be explained by a higher activity of this catalyst in the water gas shift reaction due to the positive effect of Pr cations, which also helps to provide a higher activity in ethanol reforming (a higher total concentration of products CO + CO_2 + CH_4) despite the identical density of isolated active metal sites stabilizing terminal carbonyls (vide supra). Although, for this catalyst hydrogen content increases with temperature correlating with the decrease of the methane byproduct content (Figure 16), at 700°C, it is slightly less than that observed for the La-containing catalyst (~7% versus ~8.6%). This apparently correlates with the decrease of CO_2 content with temperature due to the

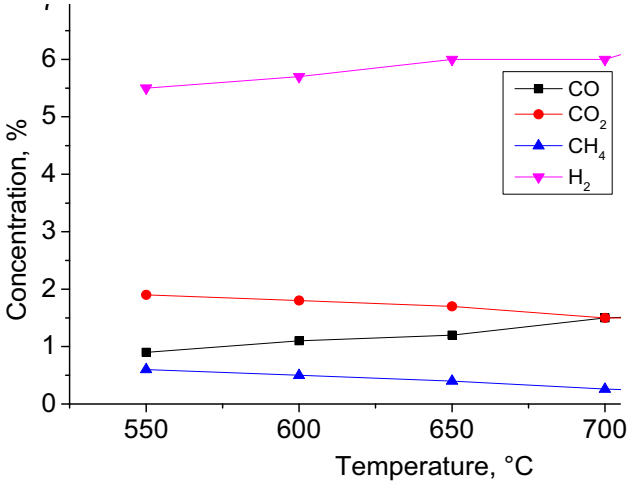

Figure 16: Temperature dependencies of reaction product concentrations in the process of ESR on the Ru + Ni/($MgAl_2O_4$ + $PrFe_{0.7}Ni_{0.3}O_3$) catalyst. Feed: 2% EtOH + 8% H_2O + N_2; contact time: 10 ms.

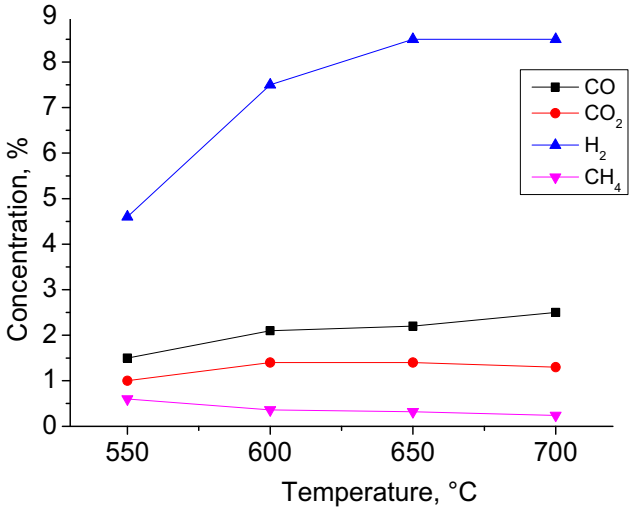

Figure 17: Temperature dependencies of reaction product concentrations in the process of ESR on the Ru + Ni/($MgAl_2O_4$ + $LaFe_{0.7}Ni_{0.3}O_3$) catalyst. Feed: 2% EtOH + 8% H_2O + N_2; contact time: 10 ms.

Table 3: Comparison of catalyst performance in ESR

Catalyst	SSA, (m^2)/g	Feed, contact time	*T* (°C)	*X* EtOH (%)	K_{eff} (s^{-1})	H_2 yield (%)	Ref.
5% Ni + 1% Ru/($MgAl_2O_4$ + $LaFe_{0.7}Ni_{0.3}O_3$)	42	2% EtOH + 8% H_2O + N_2, 10 ms	550	80	160	38	This work
5% Ni + 1% Ru/($MgAl_2O_4$ + $PrFe_{0.7}Ni_{0.3}O_3$)	83	2% EtOH + 8% H_2O + N_2, 10 ms	550	83	180	46	This work
5% Ni + 1% Ru/10% $Pr_{0.3}Ce_{0.35}Zr_{0.35}O_2$/$MgAl_{1.9}Cr_{0.1}O_4$	86	2% EtOH + 8% H_2O + N_2, 8 ms	500	40	51	47	11
5% Ni + 1% Ru/$Pr_{0.3}Ce_{0.35}Zr_{0.35}O_2$/$MgAl_{1.9}Fe_{0.1}O_4$	85	2% EtOH + 8% H_2O + N_2, 8 ms	550	98	—	51	11
NiAlVOx (Ni:Al:V = 2.07:1:0.43)	294	10% EtOH + 40% H_2O + N_2, 70 ms	400	60	13	5	20
			500	100	—	20	
10 wt% CuNiCr/10 wt% CeZrPrO/Al_2O_3	100	10% EtOH + 40% H_2O + N_2, 72 ms	650	31	5	5	21
5% Ni/50% $Pr_{0.15}Sm_{0.15}Ce_{0.35}Zr_{0.35}O_2$ + 50% $LaMn_{0.9}Ru_{0.1}O_3$	21	2% EtOH + 8% H_2O + N_2, 10 ms	500	80	160	32	19
2% Ni + 2% Ru/$MnCr_2O_4$	77	10% EtOH + 40% H_2O + He, 70 ms	500	92	36	68	22

effect of the reverse water gas shift reaction, while for the La-containing catalyst the CO_2 concentration is nearly constant due to less efficiency in this reaction.

In Table 3, a comparison of the performance of nanocomposite catalysts prepared in this work as well as those containing Ni on different supports [11,19–22] is presented. In the intermediate temperature range, the hydrogen yield and effective rate constants for nanocomposite catalysts prepared in this work using a simplified one-pot procedure are good being close to those for catalysts on doped $MgAl_2O_4$, which are among the most active and stable Ni-based catalysts of fuel reforming [11]. The higher activity of 5% Ni + 1% Ru/($MgAl_2O_4$ + $PrFe_{0.7}Ni_{0.3}O_3$) catalyst is explained by the formation of disordered Pr nickelate fragments which strongly interact with the Fe-modified spinel support. The interaction of Pr cations with metal alloy nanoparticles as well as their presence in the oxide support surface layer provide higher efficiency of ethanol activation as well as a higher concentration of reactive oxygen species on the support [3,8] which ensure the higher activity of the Pr-containing catalyst compared with that containing La. This agrees with the high activity of the 5% Ni/50% $Pr_{0.15}Sm_{0.15}Ce_{0.35}Zr_{0.35}O_2$ + 50% $LaMn_{0.9}Ru_{0.1}O_3$ catalyst [19] also containing Pr cations. The good performance of the 2% Ni + 2% Ru/$MnCr_2O_4$ catalyst is explained by the high dispersion of Ni-Ru alloy nanoparticles, which strongly interact with the $MnCr_2O_4$ support, and the high oxygen mobility and reactivity [22]. The lower performance of 10 wt% CuNiCr/10 wt% CeZrPrO/Al_2O_3 [21] is apparently explained by the low surface concentration of Ni and Pr cations incorporated into the bulk of alumina support. Note that the NiAlVOx catalyst based on layered Ni-Al-O hydrotalcite with a high Ni content at 500°C provides complete ethanol conversion with a low hydrogen yield due to domination of byproducts such as acetaldehyde, ethylene, and dimethyl ether due to the absence of other transition metal or rare earth cations having the ability to provide a high surface concentration of reactive oxygen species required to convert intermediates into syngas [20].

4 Discussion

Herein, a simple and cost-effective one-pot procedure of nanocomposite ($MgAl_2O_4$ + $LnFe_{0.7}Ni_{0.3}O_3$) preparation with subsequent loading of Ni + Ru on the support by co-impregnation allowed us to obtain efficient and stable to coking catalysts for ESR, which was provided by the optimized interaction between spinel and perovskite phases. Although these catalysts were tested here only in diluted

feed, for mesoporous catalysts based on the $MgAl_2O_4$ support, our previous studies demonstrated that a high and stable performance in this reaction in diluted feed reliably correlates with the high activity and coking/sintering stability in concentrated feeds in other reactions such as methane steam/dry reforming and biofuel steam/autothermal reforming [10,11]. This apparently provides good prospects of this preparation procedure for the design of mesoporous nanocomposite active components for structured catalysts of fuel transformation into syngas. Moreover, since a comparison of performance in reactions of methane dry reforming and ESR of our catalysts based on a doped $MgAl_2O_4$ support with that of other catalysts presented in a lot of published papers demonstrated much higher specific catalytic activity [11], there is clearly a good chance of their broad practical application, with due regard for their cost-effective composition and preparation procedure. Further studies will be devoted to improving catalysts by increasing their SSA, oxygen mobility, and reactivity by variation of their chemical composition and synthesis procedures. The first step is changing the perovskite composition by removing nickel (this will increase perovskite structure stability under reducing conditions), replacing a part of Fe by a combination of Mn, Cr, and Ti and using a combination of La, Pr, and Sm instead of pure La or Pr. This will help create high entropy perovskite nanoparticles possessing higher stability along with higher oxygen mobility [23,24]. To increase the SSA, the content of perovskites in nanocomposites can be somewhat decreased (up to 40 wt%), but a part of Al (up to 10%) in spinel can be replaced by Fe, Cr, and Ti [11] or their combinations to ensure stability of perovskites phases in these nanocomposites. The second step is optimization of the one-pot synthesis procedure with application of spray drying of polymeric solution and calcination of nanopowders in a tubular reactor in the air stream, which will help prevent nanoparticle sintering. The next logistic step is supporting optimized active components on structured heat-conducting substrates from their suspensions and their testing in fuel reforming into syngas in concentrated feeds [10,14].

5 Conclusions

A cost-effective one-pot procedure of mesoporous nanocomposite $MgAl_2O_4$ + $LnFe_{0.7}Ni_{0.3}O_3$ (Ln = La, Pr) synthesis with the Pluronic P123 copolymer was applied for the first time. A disordered structure of obtained nanocomposites was formed due to incorporation of transition metal cations into the spinel structure. This provides strong interaction of the Ni + Ru active components loaded by wet co-impregnation with these nanocomposite supports, leading to uniform spatial distribution and decoration of metal alloy nanoparticles in reduced catalysts by oxidic fragments. This leads to a developed metal–support interface and domination of single surface metal centers, as demonstrated by a unique and reliable method such as FTIRS of adsorbed CO. The ESR reaction results in high catalytic activity close to that of best catalysts based on $MgAl_2O_4$ and stability to coking. A higher yield of hydrogen at 550°C for the Pr-containing catalyst is obtained by the higher reactivity of surface oxygen species bound with Pr cations.

Funding information: This work was supported by the project FWUR-2024-0033 of the Russian Federation Ministry of Science and Higher Education. The authors acknowledge the Shared Research Center “VTAN” of the Novosibirsk State University supported by the Ministry of Science and Higher Education of the Russian Federation by agreement #075-12-2021-697 for TEM investigations.

Author contributions: Conceptualization: V.S. and B.M.; investigation: N.T., J.F., N.G., T.K., V.R., and A.I.; writing – original draft preparation: N.T., T.G., and T.K.; writing – review and editing: V.S.; supervision: V.S. and B.M. All authors have read and agreed to the published version of the manuscript.

Conflict of interest: The authors declare no conflicts of interest.

Ethical approval: The conducted research is not related to either human or animal use.

Data availability statement: All data generated or analyzed during this study are included in this published article.

References

[1] Xu X, Zhou Q, Yu D. The future of hydrogen energy: bio-hydrogen production technology. Int J Hydrog Energy. 2022;47:33677–98. doi: 10.1016/j.ijhydene.2022.07.261.

[2] Ogo Sh, Sekine Ya. Recent progress in ethanol steam reforming using non-noble transition metal catalysts: a review. Fuel Process Technol. 2020;199:106–238. doi: 10.1016/j.fuproc.2019.106238.

[3] Sadykov VA, Arapova MV, Smal EA, Pavlova SN, Bobrova LN, Eremeev NF, et al. Nanocomposite catalysts for transformation of biofuels into syngas and hydrogen: Fundamentals of design and performance, application in structured reactors and catalytic membranes. Catalysis. 2019;31:216–41. doi: 10.1039/9781788016971-00216.

[4] Sadykov VA, Eremeev NF, Sadovskaya EM, Chesalov YA, Pavlova SN, Rogov VA, et al. Detailed mechanism of ethanol transformation into syngas on catalysts based on mesoporous $MgAl_2O_4$ support loaded with Ru+Ni/(PrCeZrO or $MnCr_2O_4$) active components. Top Catal. 2020;63:166–77. doi: 10.1007/s11244-020-01222-1.

[5] Guo J, Cai R, Cali E, Wilson GE, Kerherve G, Haigh SJ, et al. Low-temperature exsolution of Ni–Ru bimetallic nanoparticles from A-site deficient double perovskites. Small. 2022;18:2107020. doi: 10.1002/smll.202107020.

[6] Roh H-S, Potdar H, Jun K-W, Kim J-W, Oh Y-S. Carbon dioxide reforming of methane over Ni incorporated into Ce–ZrO_2 catalysts. Appl Catal A Gen. 2004;276:231–9. doi: 10.1016/j.apcata.2004.08.009.

[7] Sadykov V, Bobrova L, Pavlova S, Simagina V, Makarshin L, Parmon V, et al. Syngas generation from hydrocarbons and oxygenates with structured catalysts. Series energy science, engineering and technology. New York: Nova Science Publishers, Inc; 2012. p. 140.

[8] Pavlova S, Kapokova L, Bunina R, Alikina G, Sazonova N, Krieger T, et al. Syngas production by CO_2 reforming of methane using $LnFeNi(Ru)O_3$ perovskites as precursors of robust catalysts. Catal Sci Technol. 2012;2:2099–108. doi: 10.1039/C2CY20054F.

[9] Naurzkulova SM, Arapova MV, Ishchenko AV, Krieger TA, Saraev AA, Kaichev VV, et al. Ni–Ru-containing mixed oxide-based composites as precursors for ethanol steam reforming catalysts: Effect of the synthesis methods on the structural and catalytic properties. Open Chem. 2021;19:696–708. doi: 10.1515/chem-2021-0062.

[10] Sadykov V, Pavlova S, Fedorova J, Bobin A, Fedorova V, Simonov M, et al. Structured catalysts with mesoporous nanocomposite active components loaded on heat-conducting substrates for transformation of biogas/biofuels into syngas. Cat Today. 2021;379:166–80. doi: 10.1016/j.cattod.2020.10.017.

[11] Sadykov VA, Eremeev NF, Sadovskaya EM, Fedorova JE, Arapova MV, Bobrova LN, et al. Approaches to the design of efficient and stable catalysts for biofuel reforming into syngas: Doping the mesoporous $MgAl_2O_4$ support with transition metal cations. Dalton Trans. 2023;52:8756. doi: 10.1039/d3dt00830d.

[12] Paukshtis EA, Yurchenko EN. Study of the acid-base properties of heterogeneous catalysts by infrared spectroscopy. Russ Chem Rev. 1983;52:242–58. doi: 10.1070/RC1983v052n03ABEH002812.

[13] Coluccia S, Baricco M, Marchese L, Martra G, Zecchina A. Surface morphology and reactivity towards CO of MgO particles: FTIR and HRTEM studies. Spectrochim Acta A. 1993;49:1289–98. doi: 10.1016/0584-8539(93)80036-A.

[14] Sadykov V, Pavlova S, Smal E, Arapova M, Simonov M, Mezentseva N, et al. Structured catalysts for biofuels transformation into syngas with active components based on perovskite and spinel oxides supported on Mg-doped alumina. Catal Today. 2017;293–294:176–85. doi: 10.1016/j.cattod.2017.05.055.

[15] Hadjiivanov K, Mihaylov M, Abadjieva N, Klissurski D. Characterization of Ni/TiO_2 catalysts prepared by successive adsorption-reduction of Ni^{2+} ions. J Chem Soc Faraday Trans. 1998;94:3711–6. doi: 10.1039/A804978E.

[16] Jensen MB, Morandi S, Prinetto F, Olafsen Sjastad A, Olsbye U, Ghiotti G. FTIR characterization of supported Ni-catalysts: Influence of different supports on the metal phase properties. Catal Today. 2012;197:38–49. doi: 10.1016/j.cattod.2012.06.016.

[17] Chen HW, Zhong Z, White JM. CO chemisorption on Ru/SiO_2: The influence of coadsorbates. J Catal. 1984;90:119–26. doi: 10.1016/0021-9517(84)90092-7.

[18] Mihaylov M, Lagunov O, Ivanova E, Hadjiivanov K. Determination of polycarbonyl species on nickel-containing catalysts by adsorption of CO isotopic mixtures. Top Catal. 2011;54:308–17. doi: 10.1007/s11244-011-9661-6.

[19] Arapova M, Naurzkulova S, Krieger T, Rogov V, Sadykov V. Efficient catalysts of ethanol steam reforming based on perovskite-fluorite nanocomposites with supported Ni: Effect of the synthesis methods on the activity and stability. Catalysts. 2022;12:1151. doi: 10.3390/catal12101151.

[20] Korneeva EV, Kardash TY, Rogov VA, Smal EA, Sadykov VA. Catalytic steam reforming of ethanol over W-, V-, or Nb–modified Ni-Al-O hydrotalcite-type precursors. Catal Sustain Energy. 2017;4:17. doi: 10.1515/cse-2017-0004.

[21] Yaseneva P, Pavlova S, Sadykov V, Alikina G, Lukashevich A, Rogov V, et al. Combinatorial approach to the preparation and characterization of catalysts for biomass steam reforming into syngas. Cat Today. 2008;137:23. doi: 10.1016/j.cattod.2008.03.016.

[22] Smal EA, Simonov MN, Mezentseva NV, Krieger TA, Larina TV, Saraev AA, et al. Spinel-type $Mn_xCr_{3-x}O_4$-based catalysts for ethanol steam reforming. Appl Catal B: Environ. 2021;283:119656. doi: 10.1016/j.apcatb.2020.119656.

[23] Wang Y, Liu J, Song Y, Yu J, Tian Y, Robson MJ, et al. High-entropy perovskites for energy conversion and storage: Design, synthesis, and potential applications. Small Methods. 2023;7:2201138. doi: 10.1002/smtd.202201138.

[24] Pretschuh P, Egger A, Bucher E. Crystal structure, electronic conductivity and oxygen exchange kinetics of high-entropy perovskites $La_{0.2}Pr_{0.2}Nd_{0.2}Sm_{0.2}Sr_{0.2}Co_{1-x}Fe_xO_{3-\delta}$ (x = 0, 0.5, 1). Solid State Ion. 2024;417:116705. doi: 10.1016/j.ssi.2024.116705.